MICROSTRUCTURAL ANALYSIS OF 3D PRINTED 316L STAINLESS STEEL

Jeet Parikh

Bachelor of Engineering
Mechanical Engineering
Department of Engineering
Macquarie University

Supervisor: Dr Nicholas Tse

Commonwealth Scientific and Industrial Research Organisation (CSIRO)
Manufacturing
Lindfield, NSW

CSIRO Supervisor: Dr Christophe Comte

November 6th 2017

Statement of Candidate

I, Jeet Parikh, declare that this report, submitted as part of the requirement for the award of Bachelor of Engineering in the Department of Engineering, Macquarie University, is entirely my own work unless otherwise referenced or acknowledged. This document has not been submitted for qualification or assessment at any academic institution.

Student's Name: Jeet Parikh

Student's Signature: Jeet Parikh (Electronically Signed)

Date: November 6th, 2017

Abstract

This study investigates the important, rapidly emerging, latest manufacturing technology which is revolutionising the manufacturing industries. Additive manufacturing (AM) also referred to as 3D printing, in comparison to the traditional subtracting manufacturing techniques, involves manufacturing a part by depositing material layer by layer until the final product is achieved. Once the 316L stainless steel part is printed, microstructural crystal grain analysis of the part will be carried out on the longitudinal and latitudinal cross-sectional surfaces with varying heights and comparing the results obtained with that of conventional manufacturing methods being currently used.

Table of Contents

1. Introduction

Additive manufacturing (AM) also referred to as 3D printing is revolutionising the manufacturing industries. This process involves manufacturing a part by depositing material layer by layer until the final product is achieved. There is a wide array of different AM technologies that can make a part layer-by-layer including material extrusion, powder bed fusion, binder jetting, material jetting, vat photo-polymerisation, directed energy deposition and sheet lamination [1]. It is the new rapid prototyping technique which allows for effective fabricating of various complex designs.

The traditional approach to manufacturing components is subtractive manufacturing, which removes excess material from bulk to obtain the required dimension. Additive manufacturing on the other hand inserts material layer by layer to achieve a similar if not the same result. Furthermore, Additive Manufacturing is free of constraints which are applied to traditional manufacturing in terms of the design methods and rules [2]. Classical AM first emerged from Charles Hull's research in the mid 1980's using the stereolithography apparatus to cure a photopolymer resin into stacked layers with the aid of a laser.

In additive manufacturing, complexity is generally achievable. As the product is made layer-by-layer, the cost and time taken to develop a complex part is essentially the same as that for a simple part. In comparison to conventional methods of manufacturing, the following complexities are possible [1]:

- Features: "undercuts, variable wall thicknesses, and deep channels"
- Geometries: "twisted and contorted shapes", "blind holes", "high strength-to-weight ratio" geometries, high surface area to-volume ratio designs, lattices, topologically optimized organic shapes
- Parts consolidation: integrate parts that would otherwise be welded or joined together into a single printed part.
- Fabrication step consolidation: nesting parts that would be assembled in multiple steps if fabricated conventionally can be printed simultaneously as demonstrated with the ball bearings

In terms of Laser based additive manufacturing, where the part is printed layer by layer using metallic powder which is melted with intensive energy input from a focused laser beam. The variation in properties along with the height of the specimen constructed must be taken in to

accordance, due to the fact that as the height increases the distance from the heat sink decreases and hence the cooling rate will decrease. Due to this fact, it is hypothesised that with varying height the microstructures will vary too for a 3D printed part.

Along with height variations, it is also hypothesised that at the corresponding heights there will be a difference between the latitudinal and longitudinal cross-section of the specimen at those particular points. This phenomenon will be tested to investigate if there indeed is a change or like the machined bulk 316L stainless steel it will remain constant throughout the sample.

In this project, working in conjunction with CSIRO and their industrial partners, the aim is to investigate the microstructures of final 3D printed 316L stainless steel, compare it to the traditional/conventional method of manufacturing being carried out currently.

1.1 Goals of this Project

In order to successfully fulfil our aim in investigating the internal structures for additive manufacturing of metal and metal based alloys we must carry out an investigation. In this investigation we will be carrying out the additive manufacturing process to produce a part with certain dimensions, then examining the corresponding microstructures to obtain a better understanding of the properties and crystal grain structure of the part.

Throughout the investigation, there will be certain tasks which are carried out in order to obtain the results needed to ensure the aims have been met. These include:

- Synthesize a bulk metal alloy from bulk powder using laser based additive manufacturing methods – Eg: Powder Bed Fusion-laser/Direct laser Deposition
- Prepare the part produced using proper preparation techniques for examination
- Examine the microstructures and crystal structure using the scientific equipment
- Accurate data compilation and analysis to publish findings

2. Background and Literature Review

2.1 Direct Laser Deposition (DLD)

The laser based additive manufacturing method used by CSIRO Lindfield, where all the research will be undertaken, is Direct Laser Deposition (DLD). DLD utilizes powder preforms that are directly deposited to a work site accompanied with simultaneous irradiation of a laser beam [7]. It includes a moving substrate, which then outputs a pool of molten metal that travels in space/time – creating the final 3-dimensional part. In figure 3 below, there is a deposition head which consists of either a single powder-spray nozzle or multiple nozzles, and in line with the head is a focused laser beam. As the powder particles are fed into the head, the laser beam provides the thermal energy required to melt the particles and the substrate along the deposition path and output it to create the desired product [7]. This creates a molten pool of the liquid metal once output. Located at the area around contact is a heat affected zone (HAZ) with varying penetration depth. Once one layer of the material has been completed successfully, the CNC relative moving substrate travels in the desired direction according to the command prompt to achieve the required shape/dimensions of the product. The system can be monitored through the use of infrared cameras or pyrometers [7].

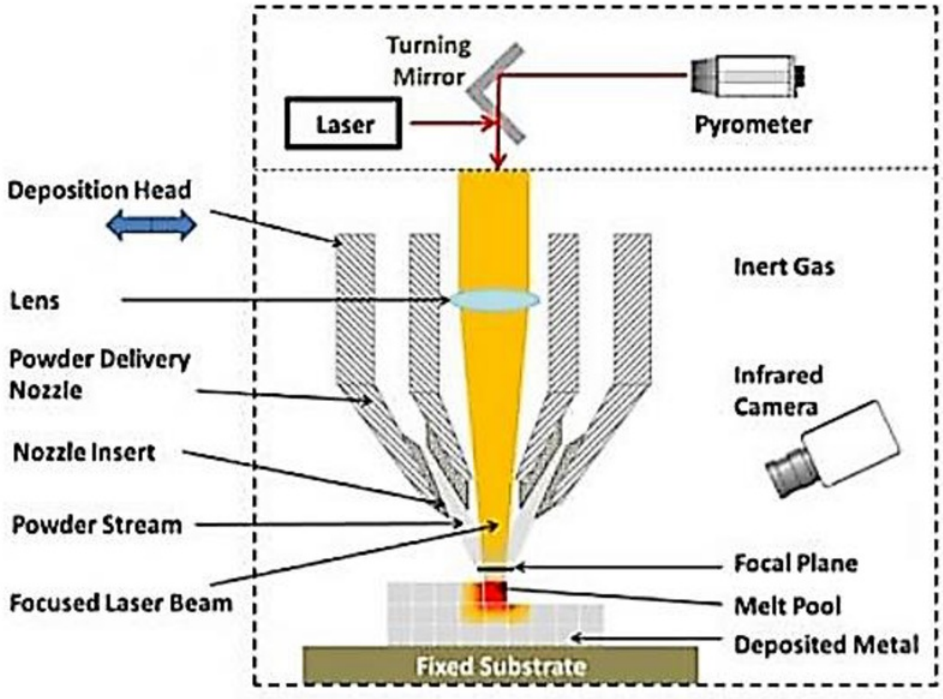

Figure 1: Blown powder Direct Laser Deposition (DLD) with thermal monitoring. Adapted by [7]

This method delivers comparable strength, accuracy (50 to 100μ) and surface roughness (<10μ). This procedure is also very useful in making once-off products (spare parts), low volume production, customized & complex products and cheap high-value products (medical implants) as well as rapid prototyping in terms of design for any project [10]. It is specifically notable for application in the following fields: medical, aerospace, automotive, jewellery and tooling.

2.2 Printing Parameters

A. Speed and Layer Thickness of Print

An investigation was undertaken by K. Christiyan, U. Chandrasekhar and K. Venkateshwarlu [4] to determine the tensile strength for 3-d printed metals with variations in the layer thickness, printing speed and nozzle diameter. The following figure shows the relationship between strain and strain for the specimen at the various print speeds. They suggest that with higher print speeds the stiffness of the specimen decreases and is less ductile. It was also noticed in the investigation that the tensile stress is decreased with increase in layer thickness as well as with an increase in printing speed it decreases.

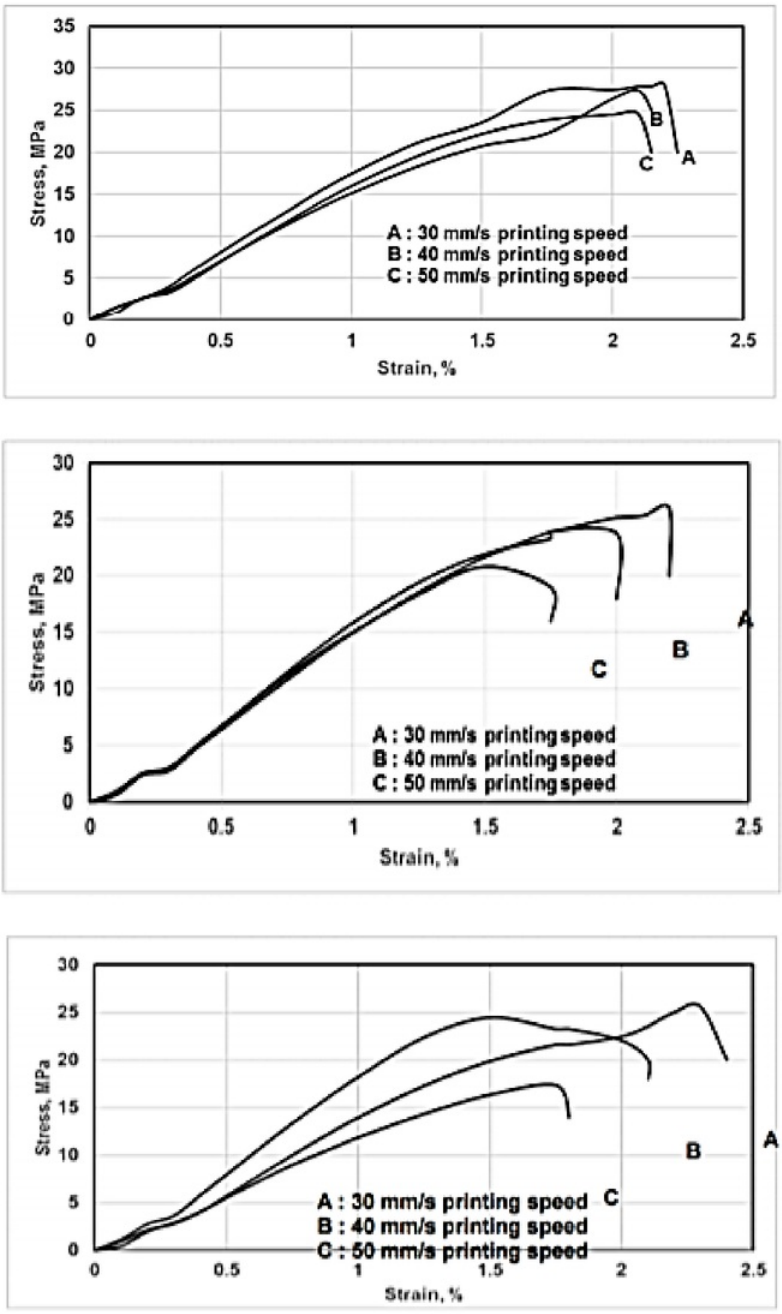

Figure 2: Tensile behaviour with 0.20mm (Top), 0.25mm (Middle), 0.30mm (Bottom) layer thickness. Adapted from [4]

2.3 Geometries

A study conducted for the Laser institute of Australia © on the characteristics of typical geometrical features shaped by a laser based additive manufacturing technique. In this paper, the authors investigated the characteristics of typical geometric features of the additive manufacturing techniques [6]. To do this, the authors designed geometric features on a 3D model such as square holes, sharp corners, thin plates, tetrahedrons and round holes as well which were printed parallel and vertical to the Z axis [6].

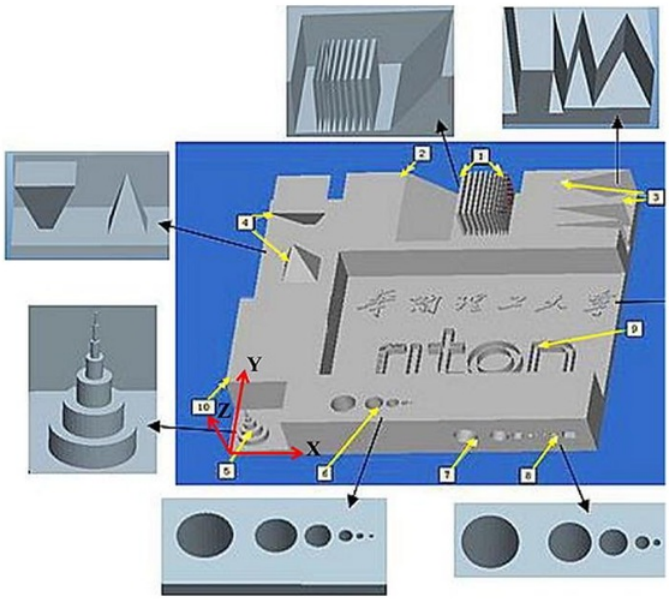

Figure 3: 3D model with typical geometric features. Adapted from [6]

The figure above shows the design structure of the various features the authors developed in their model for the investigation. The paper concluded, after considering the experiments conducted, that engineers while designing should avoid creating smaller geometric features. This includes avoiding thin plates – less than 0.2mm in thickness, cylinders with a diameter smaller than 0.3mm, overhanging round holes with a diameter less than 0.5mm [6]. If these restrictions are not implemented, the overall design may possess defects.

2.4 Solidification Process

During the additive manufacturing process, the powder material is exposed to laser energy which melts it into molten metal. Once the powders are fully melted by the laser beam, they form the melt pool, which upon contact with the previously deposited material will successfully solidify and the depositing head then carries on moving towards the completion of the part being made. The contact between the 3D printed material and the substrate induces more rapid layer and component cooling and solidification.

The melted metal is deposited initially onto a substrate, this wets the respective substrate and due to the surface tension of the substrate the thermal effect of the melt pool will spread around the beam path. This capillary-driven motion and the thermal transport of the melt pool into the substrate leads to the total width of the melt track that is typically 2 to 3 times that of the incoming incident laser beam [14].

The internal structure of the metal being deposited follows columnar growth features near the center of the melt pools and cylindrical-like microstructural features at the melt pool edges, respectively; corresponding to temperature variances or gradients. The liquid/solid interface becomes a connected 2-dimensional array of distinct thermal gradients which produce directional microstructures: columnar or oriented (textured) grains and other directional microstructures simultaneously [15].

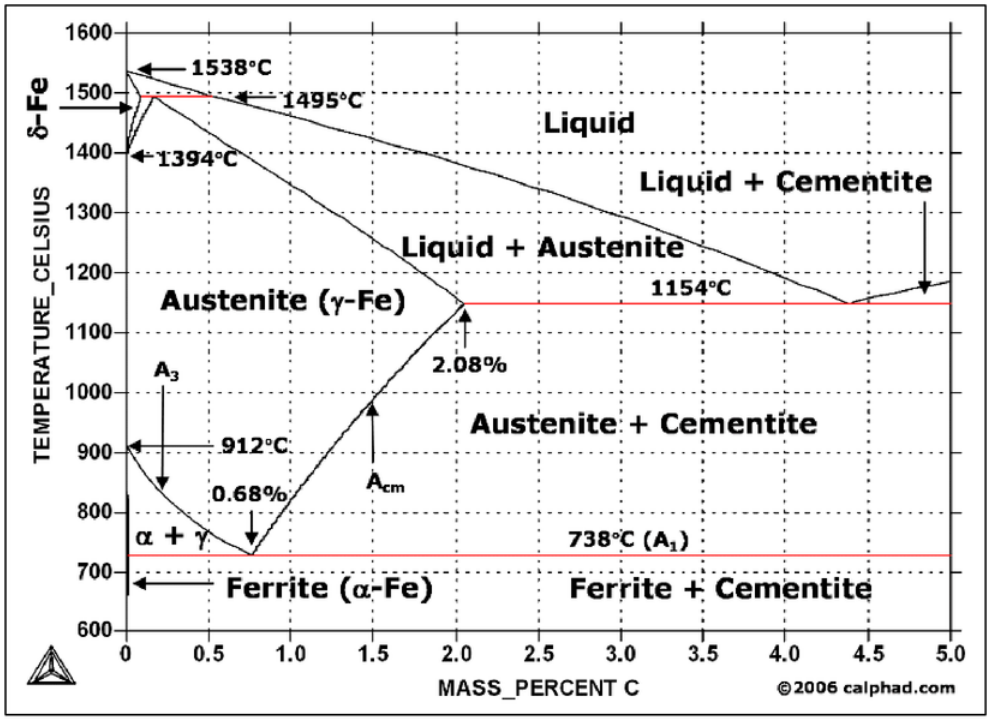

Figure 4: Typical Iron-Carbon (Fe-C) Phase Diagram. Adapted from [18]

The Fe-C diagram above shows which phases are to be expected at equilibrium (or metastable equilibrium) for different combinations of carbon concentration and temperature.

The powdered 316L stainless steel powder is being deposited and melted at 1400ºC using the laser energy. Once the part is printed, the internal phase of the material is in the austenitic region, with austenite grains forming. The molten metal interaction with the substrate, cools the total deposited part and then thermal equilibrium at the interface between the deposited material and the substrate result in a austenitic and ferritic internal structure of the part.

2.3 Annealing heat treatment process

Steels can be heat treated to produce a great variety of microstructures and properties. The heat treatment process uses phase transformation during the heating and cooling processes to change a microstructure in a solid state.

Annealing is a heat treatment process which involves treating steel up to a high temperature, then cooling it very slowly to room temperature, so that the resulting microstructure will possess high ductility and toughness, but low hardness. Annealing is performed by heating a component to the appropriate temperature, soaking it at that temperature and then letting it cool down itself with the air. This process produces structures according to the Fe-Fe_3C diagram, in a state of equilibrium.

In a study conducted by N. Tsuji et al. 1100-Al specimens are annealed for 1.8ks at various temperatures ranging from 373K to 573K. TEM microstructures of the annealed 1100 aluminium are shown in the figure below. It is clearly observed from this investigation's results that at the 373K temperature there are long, thin and more consistent columnar grains. With increasing annealing temperature, it is examined the grains gradually grew as well correspondingly. Towards the end, above the 523K temperature range, the crystal grains are revealed to be of equiaxed morphology with no dislocation substrates inside [19].

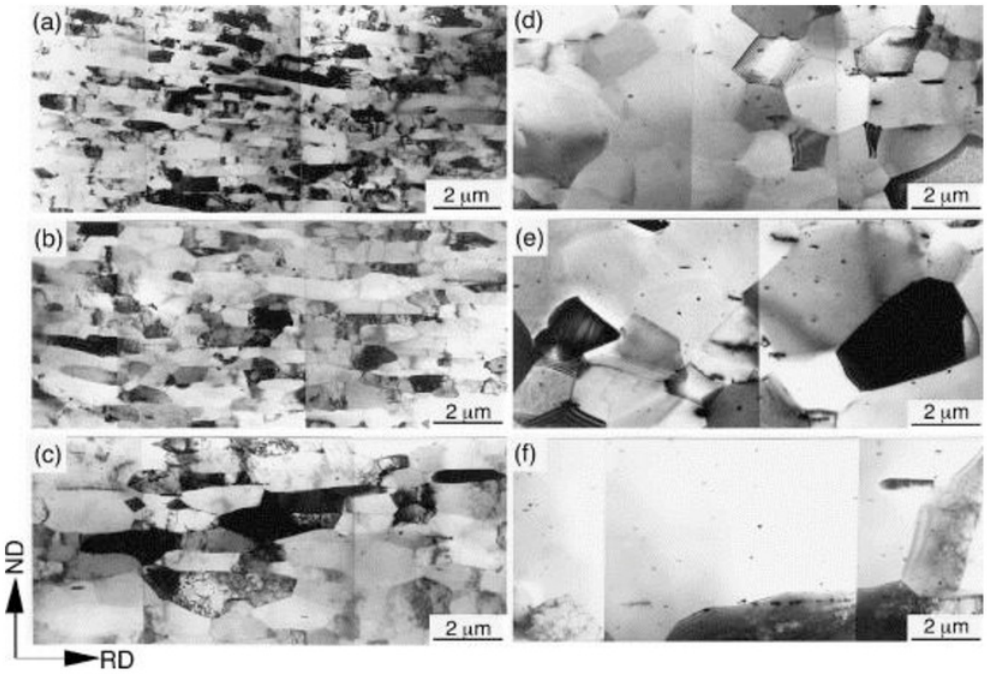

Figure 5: TEM microstructures of the 1100 Aluminium annealed for 1.8ks at (a) 373 K, (b) 423 K, (c) 473 K, (d) 498 K, (e) 523 K and (f) 573 K. Adapted from [19]

Isothermal annealing is the heat addition process undergone to produce uniform ferritic and pearlitic structures. In a general isothermal annealing process, the product after austenising taken directly to the annealing furnace maintained below lower critical temperature and hold isothermally till the pearlitic reaction completes as shown in figure. The initial cooling of the products such that the temperature at the centre and surface of the material reach the annealing temperature before incubation period of ferrite. As the products are held at constant temperature, constant undercooling will allow for the grain size of ferrite and interlamellar spacing of pearlite to be uniform. The overall cycle time is lower than that required by full annealing [16].

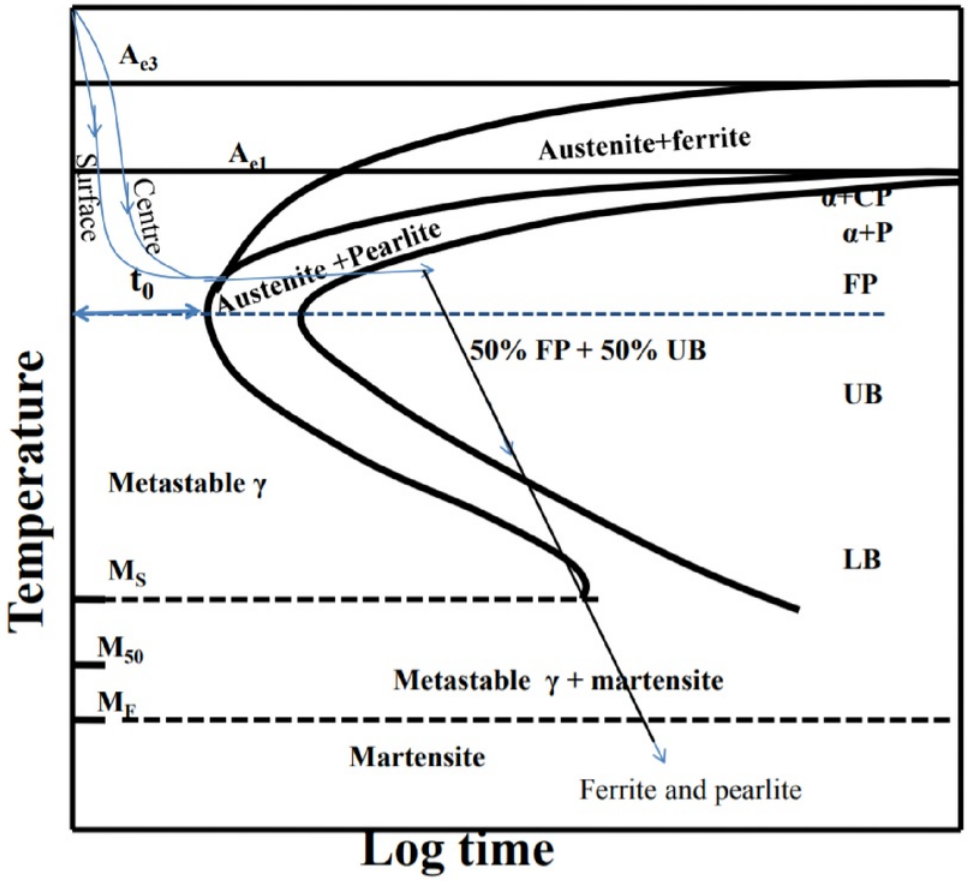

Figure 4: Isothermal annealing heat treatment superimposed on TTT diagram. Adapted from [16]

The cooling rate after finishing deformation stage has a significant effect on the mechanical properties through engendering a variety of microstructure constituents that alter significantly the mechanical properties. Higher cooling rates lead to a decrease of ferrite grain size and formation of high strength, hardness, dislocation density, and fine phases because it suppresses the atomic diffusion. Whereas slow cooling rates lead to transformation into soft, coarse and less dislocated phases like polygonal ferrite [17].

2.5 Electron Backscatter Diffraction (EBSD)

Electron Backscatter Diffraction is the scanning an electron microscope process which reveals the crystallographic information regarding the sample's microstructure. In this technique, a fixed electron beam interacts with a crystalline sample which has been properly tilted, allowing for the electrons to be diffracted form a diffraction pattern to be detected by a fluorescent screen. The diffraction pattern highlights the crystalline structure, grain boundaries and orientation of the sample [8].

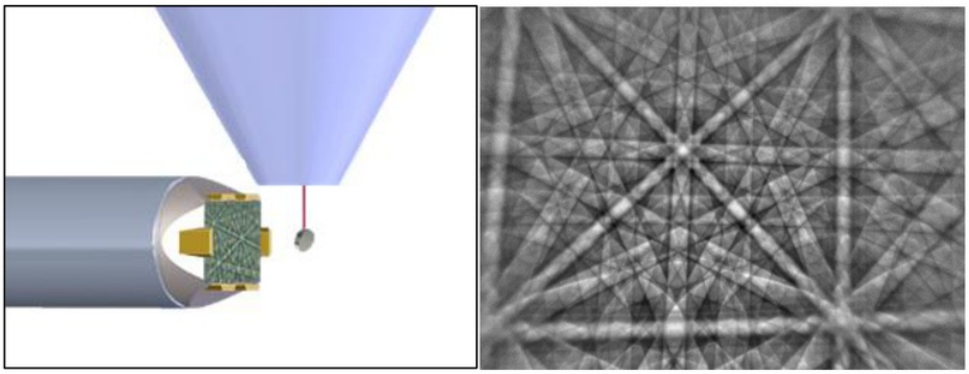

Figure 6: Schematic of EBSD process (LEFT) and a typical diffraction pattern for nickel (RIGHT). Adapted from [9]

The EBSD technique permits microstructural analysis, this is important as it illustrates many of the physical properties the material possesses. For example, properties of grain boundaries can determine the way in which materials fracture and the grain size can influence tensile strength. EBSD is used to form crystal orientation maps, points with similar crystal orientations are shown in similar colours and a grain in this map is defined as a region of the sample where the crystal orientation is the same within a certain orientation angle tolerance. These maps accurately display all position of grains and their corresponding grain boundaries.

The optimal arrangement results when the camera is as close to the sample as possible while avoiding the possibility of collision between the sample surface and the delicate phosphor screen. The phosphor screen then converts the diffracted electrons into light suitable for the CCD camera to record. Specialized computer software analyses the electron back scattered pattern by detecting the number of Kikuchi bands using an optimized Hough transform [11].

The data obtained is used to index the pattern, to identify the phase and to determine the orientation of the crystal from which the pattern was generated.

The technique works by placing a polished sample in the SEM and inclining it at approximately 70º relative to the normal incidence of the electron beam. The detector is generally a camera with a phosphor screen attached, integrated with a digital frame grabber. The camera is housed within motorized carriage which allows for it to be inserted within 20mm of the surface of the inclined sample. The optimal arrangement results when the camera is as close to the sample as possible while avoiding the possibility of collision between the sample surface and the delicate phosphor screen. [12].

When the primary laser beam interacts with the crystal lattice, the low energy loss backscattered electrons are channelled and are subject to differences in path which then lead to interferences, constructive and destructive. Once the phosphor screen is accordingly placed a short distance from the tilted sample, in the path of the diffracted electrons, a diffraction pattern is captured in the detector camera [11].

2.6 Preparation of the Sample

For this investigation, we will be analysing the specimen created using an SEM. Hence it is crucial that the specimen is prepared correctly since its preparation highlights the true representation of the sample itself.

1) Techniques for Preparation

The first step obviously is to cut the specimen to the correct size and then to grind and polish the surface to reveal the various features of the specimen. The correct size depends on the microscope being used, generally a few centimetres with the thickness being extremely low [3].

After the sample has been cut appropriately, the surface of the specimen is then grounded and polished to level it, ensuring it is uniform throughout the region of interest [3]. To aid this process, the cut specimen can then be either compression-moulded or cold-mounted in a polymer mould, which helps to keep the specimen secure while polishing and protect the specimen from breaking [3].

To ensure the specimen is prepared accurately, further finer polishing of the sample is undergone. This step involves grinding the surface with an abrasive paper or cloth, starting from course grit and using progressively finer and finer grit sizes [3]. A general guideline for simple materials is to start with 50-grit SiC paper and go through three or four levels, finishing with 600 grit [3]. This is followed by finer polish, Al_2O_3 suspension is recommended for most except for very hard surfaces, where diamond paste can be used. These suspensions and pastes are available with abrasives as fine as 0.05-mm particle size [3].

For each stage of polishing, deformations caused by the previous stage must be removed, hence the finer steps of polishing need to be thorough. The settings can be adjusted for the polishing wheels on which the abrasives are installed, this includes rotational speed, pressure being applied and polishing pattern as well. Once the grinding process is complete, the surface should possess no scratches or imperfections.

3. Experimental Procedures and Methods:

To understand the effects of 3D printing 316L Steel, certain experimental procedures must be carried out. From developing the 3D printed 316L stainless steel specimen, to then correctly grinding & polishing it to obtain an accurate image in the scanning electron microscope to determine the sample's crystal/microstructure and hence finally comparing it to the control – A bulk 316L machined specimen.

3.1 The reference sample

The first step to this investigation is obtaining a reference 316L stainless steel part. In this investigation, a cold rolled cylindrical 316L stainless steel rod was obtained and used.

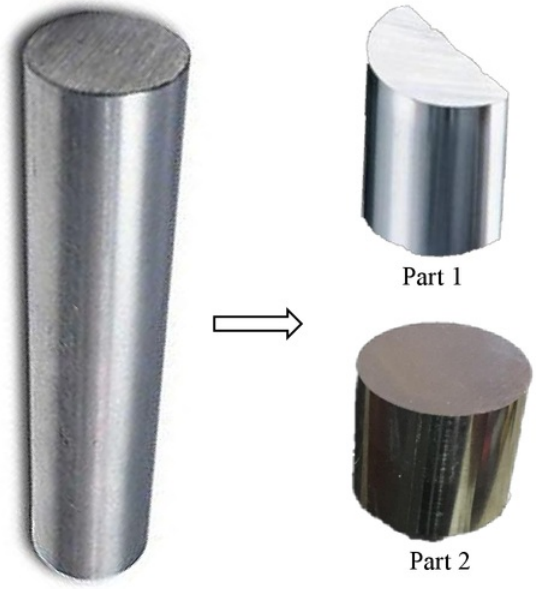

Figure 7: Reference 316L stainless steel rod and the corresponding cuts

The reference rod is used as a control to compare the experimental additive manufactured part. The sample is prepared employing the same procedure as stated below for the preparation of the 3D printed 316L stainless steel part. This part is cut according to dimensions which properly fit the mounting apparatus stated below (Struers Citopress – 10), in both the longitudinal (part 1) and latitudinal (part 2) cross-sections similar to that of the additive manufactured part as well.

3.2 Manufacturing the Part

The material used in this investigation for the additive manufacturing component was atomised spherical 316L Stainless Steel Powder. The chemical composition for the powder is given in the following table.

Table 1: Chemical Composition of the 316L stainless steel powder

Element	C	Cr	Ni	Mo	Si	Mn	Fe
At%	0.03	18.00	14.00	3.00	1.00	2.00	61.97

Once the material is obtained, the part is then constructed using the DMG MORI Lasertec 65 3D Hybrid. The machine is fed the dimensions for the part and the optimum path to be taken, which is designed using a computer aided diagram (CAD) software by the user.

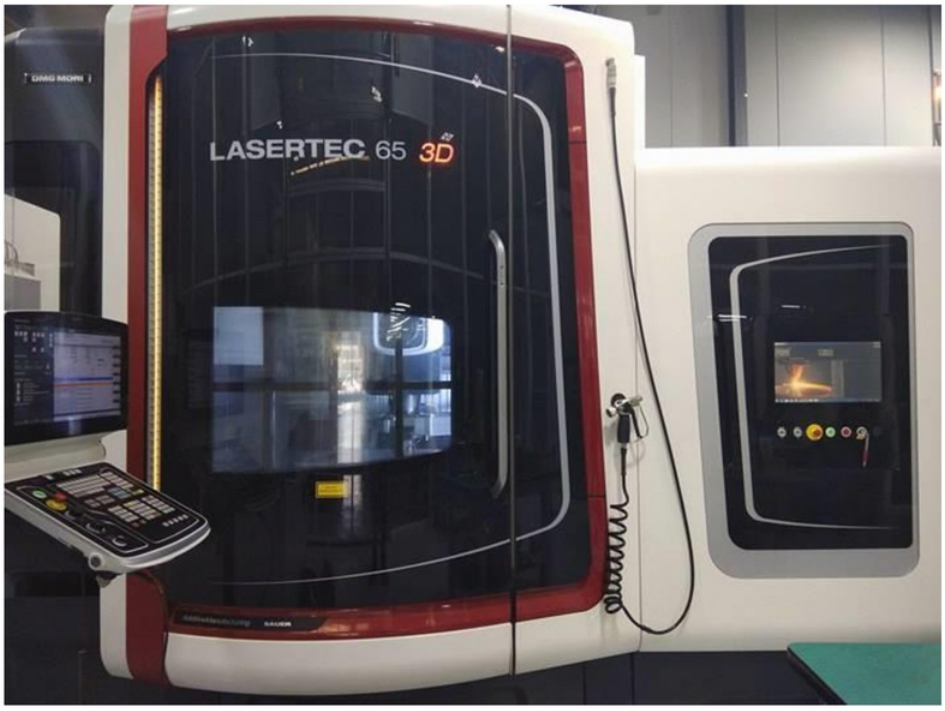

Figure 8: DMG MORI LASERTEC 65 3D HYBRID

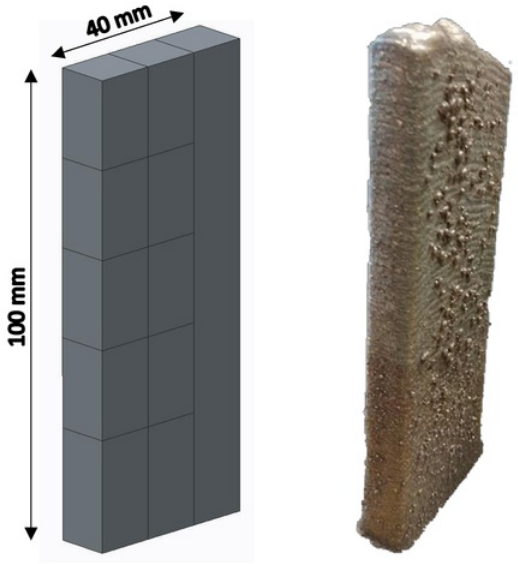

Figure 9: CAD diagram input into the machine (LEFT) with the 3D printed Output (RIGHT)

3.3 Sample Preparation

To prepare the specimen for the Scanning Electron Microscope, proper grinding and polishing is required to obtain an accurate image representation. The initial step to prepare the sample is to first cut the sample to the required size, so it can be mounted properly onto the mounting press. Figure 10 below demonstrates the process how the manufactured 3D printed part was manufactured from the computer aided diagram then cut into the 10 different sections. The shaded grey section on the right was left as excess, to visualise how the material looked internally. Each part is cut at equal lengths of 20mm each with parts 1 and 6 including the substrate within them of 5mm.

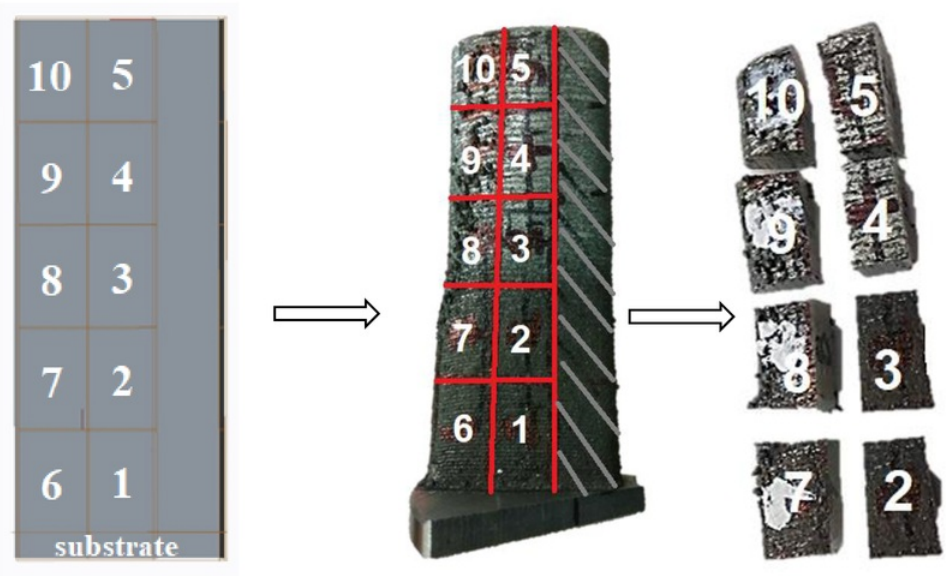

Figure 10: The manufactured part is cut appropriately for mounting

The equipmental apparatus used for cutting is the Struers Secotom - 50, high performance precision cutting tool which shapes the specimen into the corresponding dimensions with the aid of a SiC cut-off wheel, and a lubricant to ease the cutting process.

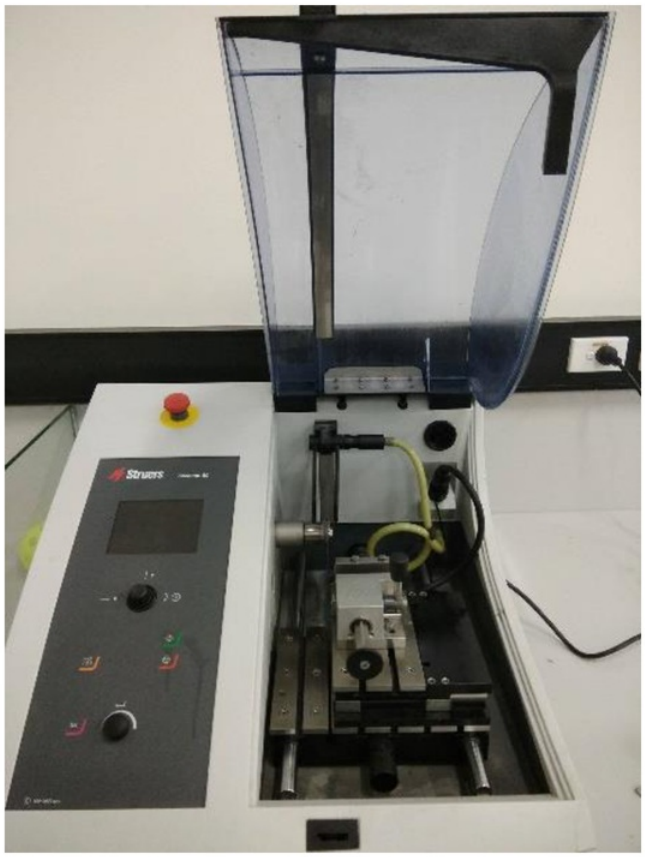

Figure 11: Figure 10: Struers Secotom – 50 sample preparation apparatus

The next step is imbedding the specimen into a mount to be compatible with the automatic polishing apparatus. For this specimen is loaded onto the Struers Citopress - 10, powerful electro-hydraulic, programmable, single cylinder hot mounting press. In this apparatus the specimen is automatically hot pressed within a thermosetting black Bakelite hot mounting resin with a carbon filler - Struers PolyFast Resin which has been especially developed for fast mounting and for examination in a SEM.

Figure 12: The Struers Citopress – 10 sample preparation apparatus

For the mounting of each of the 10 cut-off parts from the 3D print, parts 1-5 are all mounted in the latitudinal version while parts 6-10 are all mounted in the longitudinal version. This is shown in figure 13 below, the red highlighted sections are the surfaces which are being examined, hence each of the parts are mounted respectively.

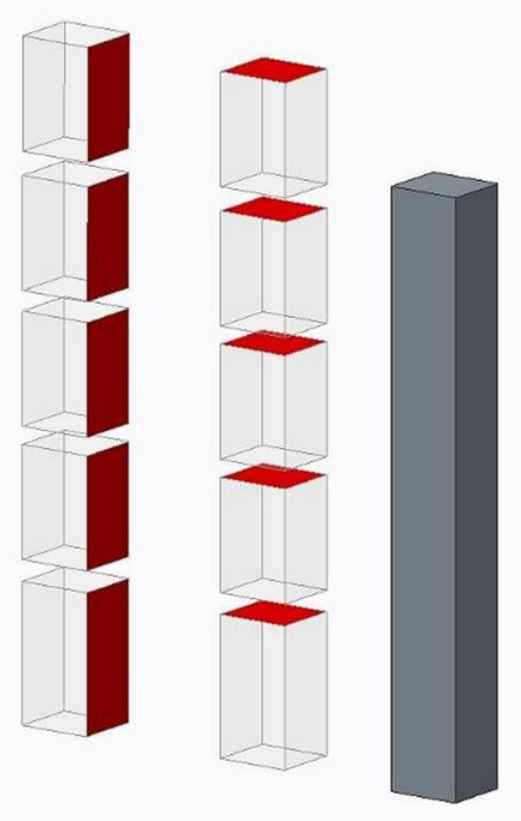

Figure 13: Exploded CAD diagram of the 3D printed part with highlighted cross sections

After the specimen has been successfully mounted with the PolyFast resin, the whole mount is then carefully loaded into the cone disc system specimen holder on the Struers Tegramin - 25. This apparatus is the main preparation system for powerful high-quality grinding and polishing of the specimen. This automated system works in 4 accurate steps corresponding to the type of material being prepared, this allows for reproducibility and precision. Since the specimen being tested is a 316 L Stainless Steel sample, which is a nickel-chromium alloy, the corresponding preparation steps taken are input into the automated system configuration and carried out as follows:

1. Coarse Grinding - SiC Foil Grinding surface at a speed of 300rpm with a 40N Force for 1 minute
2. Finer Grinding - MD-Largo Surface with a DiaPro Allegro 9 µm abrasive at a speed of 150 rpm with a 30N force for 3 minutes

3. Polishing - MD-Dac polishing surface with a DiaPro Dac 3 µm abrasive at a speed of 150 rpm with a 30N force for 3 minutes
4. Final Polishing - MD-Chem polishing surface with a OP-S 0.04 µm abrasive at a speed of 150 rpm with a 15N force for 2 minutes. This last step can be repeated multiple times in order to obtain a more perfect surface finish.

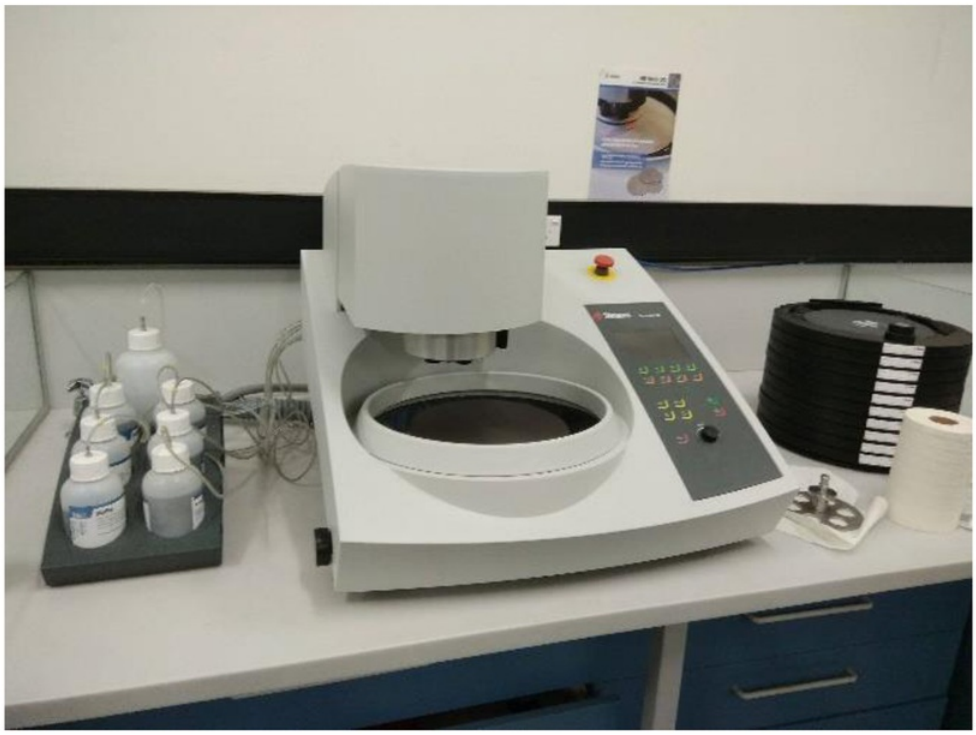

Figure 14: Struers Tegramin - 25 sample polishing apparatus

The above steps can be repeated for multiple specimens, which can be loaded onto the sample preparation system individually or simultaneously. Once the samples have been prepared meticulously, they are safely secured and stored to be taken to the Scanning electron microscope for examination.

If the above stated process does not attain the required finishing needed for sufficient results to be obtained from the scanning electron microscope analysis, the samples can be grinded and polished again further but manually this time instead of automatically by a machine. This process is quite similar to the automatic process, but this time instead of the machine carrying

out the sample preparation by instructions which have been inputted by the user, the user just carries out the same sort of stepwise grinding and polishing by using a manual powder based preparation procedure. This process includes a ceramic circular plate rotating continuously and with the help of special grit polishing powders which is layered onto the plate, the required surface finish is obtained. The various grit powders are mixed with water to create a thick paste, known as slurry, which is then spread evenly throughout the plate with the help of a brush or a similar tool. As the plate is continually spinning, the specimen surface is pressed firmly against the direction of motion of the circular plate using a head. Tap water can be used as a lubricant if needed which acts as a coolant to prevent heat build-up from friction and uniformly distributes the contact stresses between the plate and the specimen during grinding. This phenomenon refines the surface finish of the specimen as the unwanted layer of the material is slowly eradicated according to the grit size of the powder being used.

In the current investigation since the required surface finish for the samples was not obtained by the automatic polishing apparatus to show a valid result in the SEM, manual grinding had to be carried out to remove all the highly visible surface defects. The manual process used involved starting to grind the specimens with a 25μm grit alumina slurry which was layered onto the circular plate, followed by pressing each of the samples against the direction flow of motion. The samples were also moved in the head constantly rotated in the counter direction to the rotation of the circular plate to allow for even surface grinding. The above process was repeated with the 15μm alumina slurry and then a 9μm alumina slurry to match up to the first polishing stage of the automatic polishing machine. Finally, to polish the samples surface to the required finishing, each of the samples were loaded into the cone disc system specimen holder on the Struers Tegramin – 25 again and the last polishing steps (Steps 3 &4) were repeated to acquire the necessary surface finish.

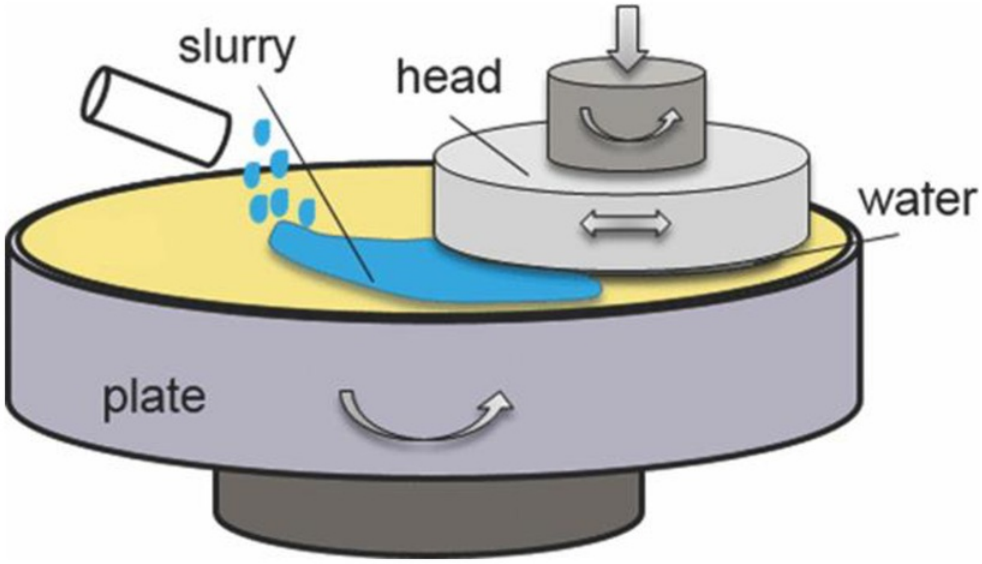

Figure 15: Schematic of the manual grinding procedure. Adapted from [13]

3.4 Scanning Electron Microscope

The Zeiss© GeminiSEM is the Scanning electron microscope (SEM) that was used for this investigation. The microscope scans a sample with a focused electron beam to deliver the images of the sample's topography and composition as well.

To install the polished samples into the SEM, the sample must first be securely attached to the mounts using gloves (to avoid contamination), carbon tabs and tightening the screws. Next loaded and locked into the side vent where it is stored and then transferred into the main area for examination.

Once the samples are shifted into the examination area, the microscope's variables are accurately calibrated to the right level after finding a point of interest. These variables include the aperture which essentially controls the sharpness of the picture by increasing or decreasing the size of the beam hitting the sample and along with that the stigmation in the x & y directions as well to control the distortions of the image being examined using the focal plan wobble. To improve the image quality, the knobs for adjusting contrast and brightness can be used as well.

Using the different lenses within the SEM, various images are observed for the varying points of interest. One of these lenses allows for a back scattered diagram to be visible, which highlights the grain structure of the material.

Furthermore, an additional attachment inserted into the SEM allow us to obtain an EBSD image of the specimen with the aid of photons, which can be analysed appropriately using appropriate software programs to deduce the samples crystal orientation and therefore its properties.

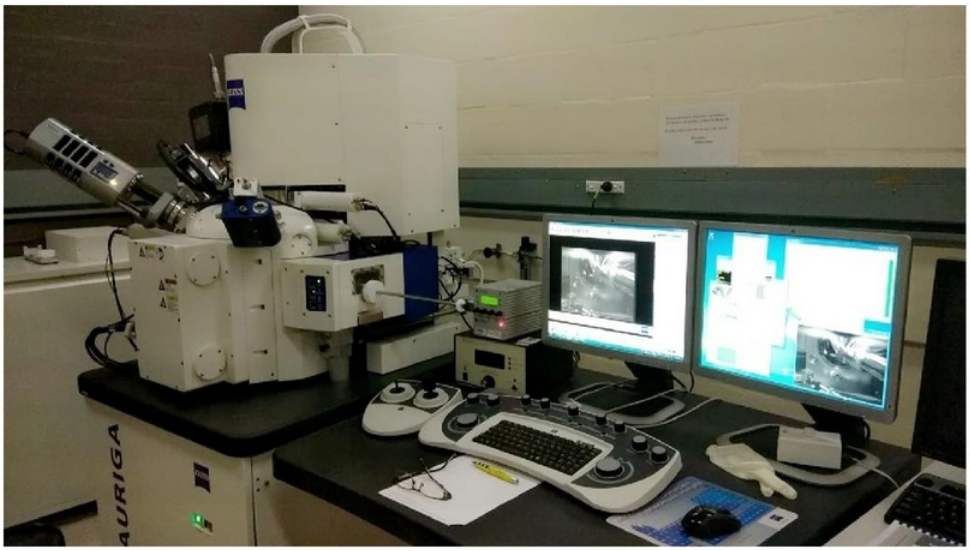

Figure 16: The Zeiss GeminiSEM scanning electron microscope

4. Results and Discussion

The results obtained from the investigation are presented below to highlight the findings. These include the scanning electron microscope images which are developed using the various lenses installed within the microscope, then examined by electron back scattered diffraction patterns to reveal corresponding crystal grain structures for each, consequently grain analysis is carried out.

4.1 Control 316L Stainless Steel Rod

The following images have been successfully obtained from the Scanning Electron Microscope for a reference bulk rolled 316 L Stainless Steel Rod. This reference sample was cut into 2 separate parts, part 1 was sliced to highlight the longitudinal cross section and part 2 was cut to highlight latitudinal cross-section as shown in figure 7. Once the polishing procedure for each part was completed, both parts were loaded individually into the SEM for inspection.

All samples are first loaded onto the scanning electron microscope and their surfaces are properly examined to highlight all key features. These key features include the grain structure which is only visible minimally

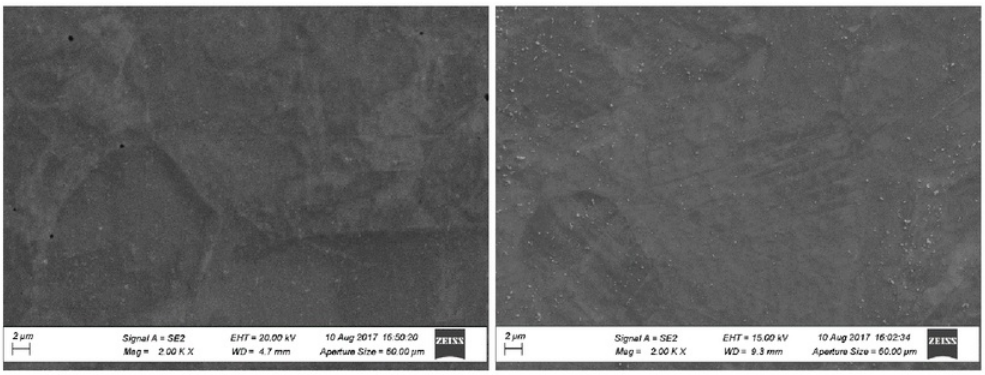

Figure 17: Images produced in the SEM highlighting the evident features in part 1

Sample 1 is the first sample of machined 316L stainless steel which was prepared and examined. This sample was sliced to highlight the longitudinal cross-section of the rolled 316L stainless steel rod.

The image produced possesses evident artefacts as observed from figure 17, these unwanted artefacts may have been developed on the surface due to imperfections which may have been still present after the vigorous polishing. Nonetheless it is still deduced from the images obtained, that the reference sample part 1 has an equiaxed grain structure.

It is also observed that debris has attached itself to the surface of the material with an average size of 104.9µm, this may have been during the transportation of the sample or after polishing during the drying stage while preparing the specimen. Along with this, pores are also developed on the surface, which may be an imperfection of the material during the manufacturing stage itself or the small sections being possibly removed during polishing stage when the part was going against the grit and the miniature sized particles attached unexpectedly scraped off.

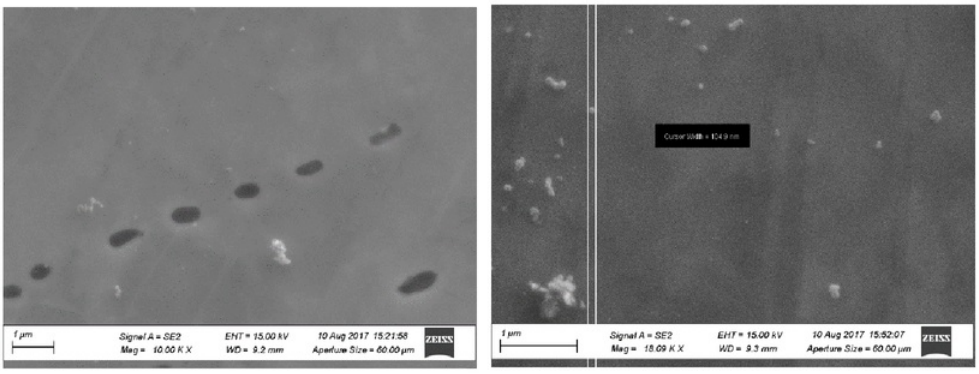

Figure 18: Magnified images from the SEM highlighting the evident artefacts on the surface of part 1 such (a) Pores (b) Dust or other unwanted debris

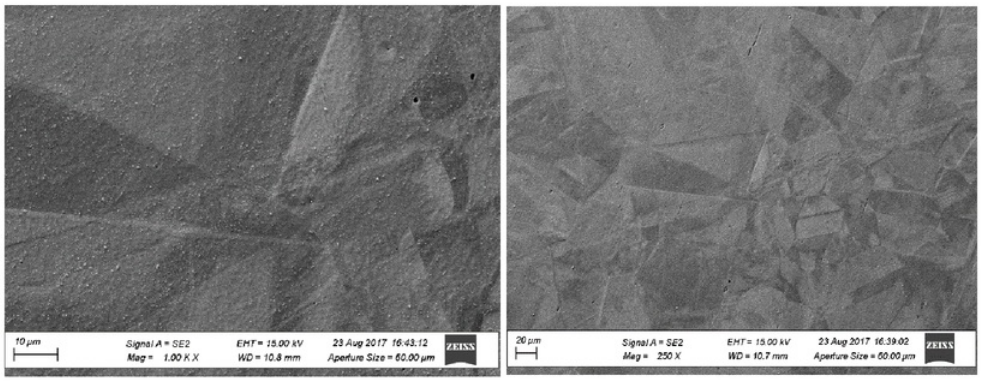

Figure 19: Images produced by the SEM to highlight evident key features along with grain structure in part 2

Part 2 is the second sample of machined 316L stainless steel which was prepared and then examined as well. This sample demonstrated the properties of the latidudinal cross-section for the reference 316L stainless steel sample.

Figure 20 below, clearly is shown to have a huge imperfection which may have developed during the polishing stage when a contaminant was pushed into a previously located pore. But nonetheless potential for EBSD pattern to be achieved since grain structure was evident in these images. Once a pattern is found, further observations can be made.

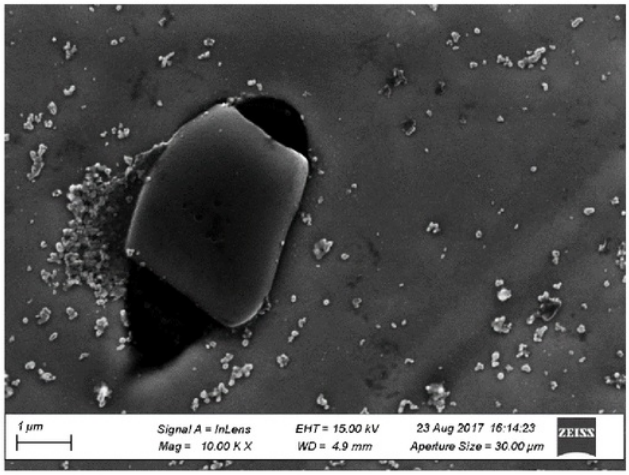

Figure 20: Highly magnified image obtained from the SEM showing the defects on the surface of part 2

Both the samples, once loaded onto the SEM were inspected with the EBSD apparatus to highlight the internal crystal structure of each. These crystal orientations are depicted below in the following figures.

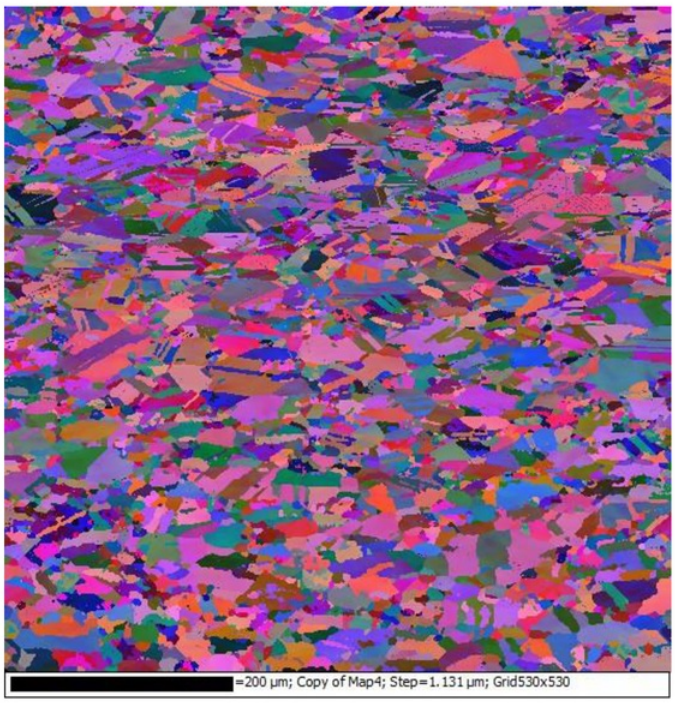

Figure 21: EBSD pattern acquired for part 1 the longitudinal 316L Reference Rod cross-section

Table 2: Crystal grain data obtained for the reference 316L stainless steel rod

	Latitudinal	**Longitudinal**
Average Area (µm²)	87.397	102.179
StDev Area (µm²)	142.923	152.647

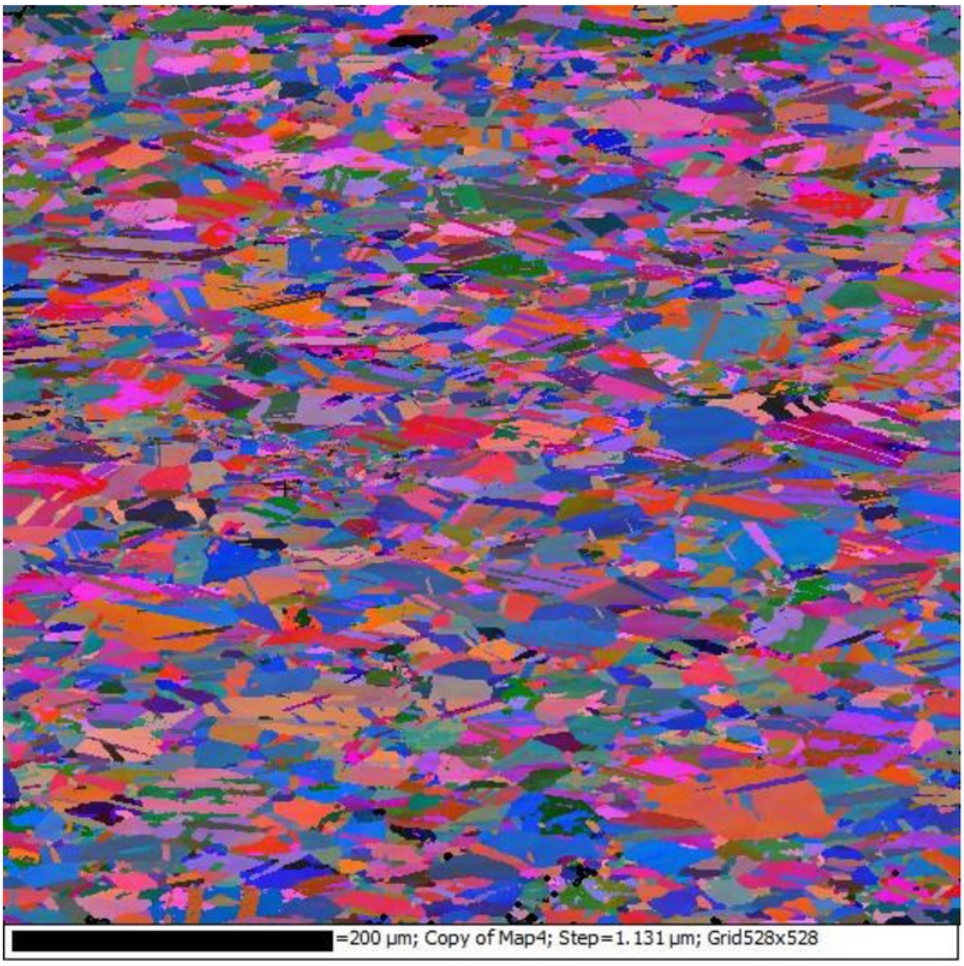

Figure 22: EBSD pattern acquired for part 1 the latitudinal 316L Reference Rod cross-section

Both figures 20-22 above illustrate an equiaxed morphology in terms of the crystal grain structure. It is observed that the grains in each of the images above, are described to be quite sharp and angular in terms of their structure. There is no considerable difference between the latitudinal and longitudinal cross-sectional crystal grain structure. Table 2 also suggests that there is a minimal difference in terms of the average grain size for the reference rod longitudinal cross-section cut which is 102.179µm², in comparison to the latitudinal cross-sectional cut which is 87.397µm². The difference is negligible and can be deduced to be of similar crystal grain size for each cut direction.

4.2 Experimentation 3D Printed Samples

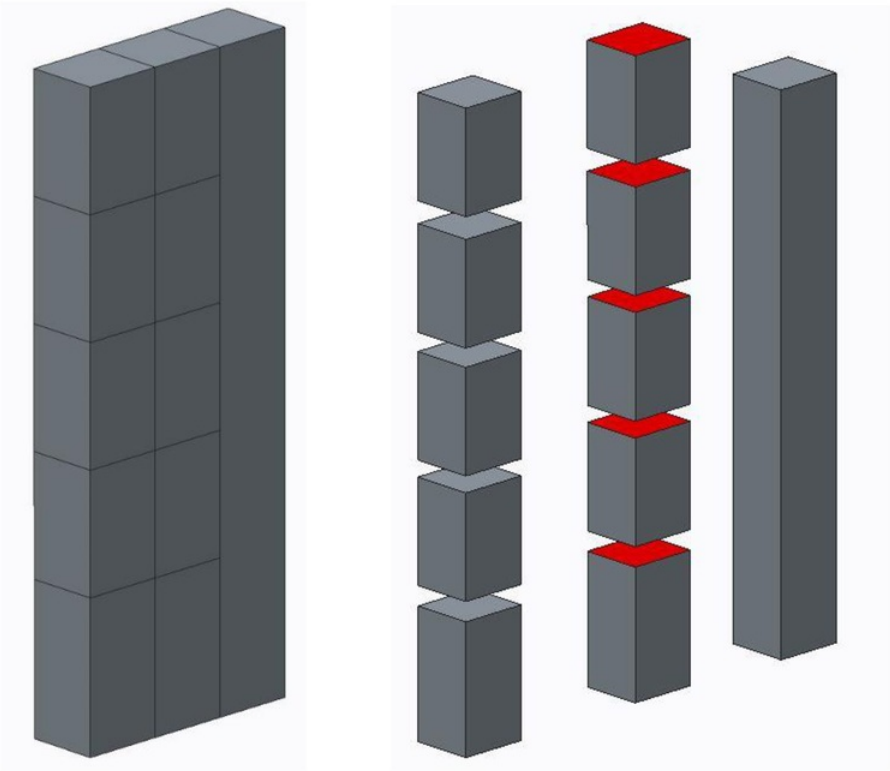

The following results have been successfully obtained using the Scanning Electron microscope (SEM) for the various 3D printed specimens. In the SEM, an additional tool was inserted to obtain the EBSD patterns of each of the parts for the sample.

All the 10 parts were not examined, as only a few would give a relevant result which can be analysed properly to determine a conclusion. The parts which were investigated include parts 1, 3, 5 in the lattitudinal direction and parts 6, 8, 10 in the longitudinal direction.

The microstructural analysis of each of those parts are presented below in the following figures and tables.

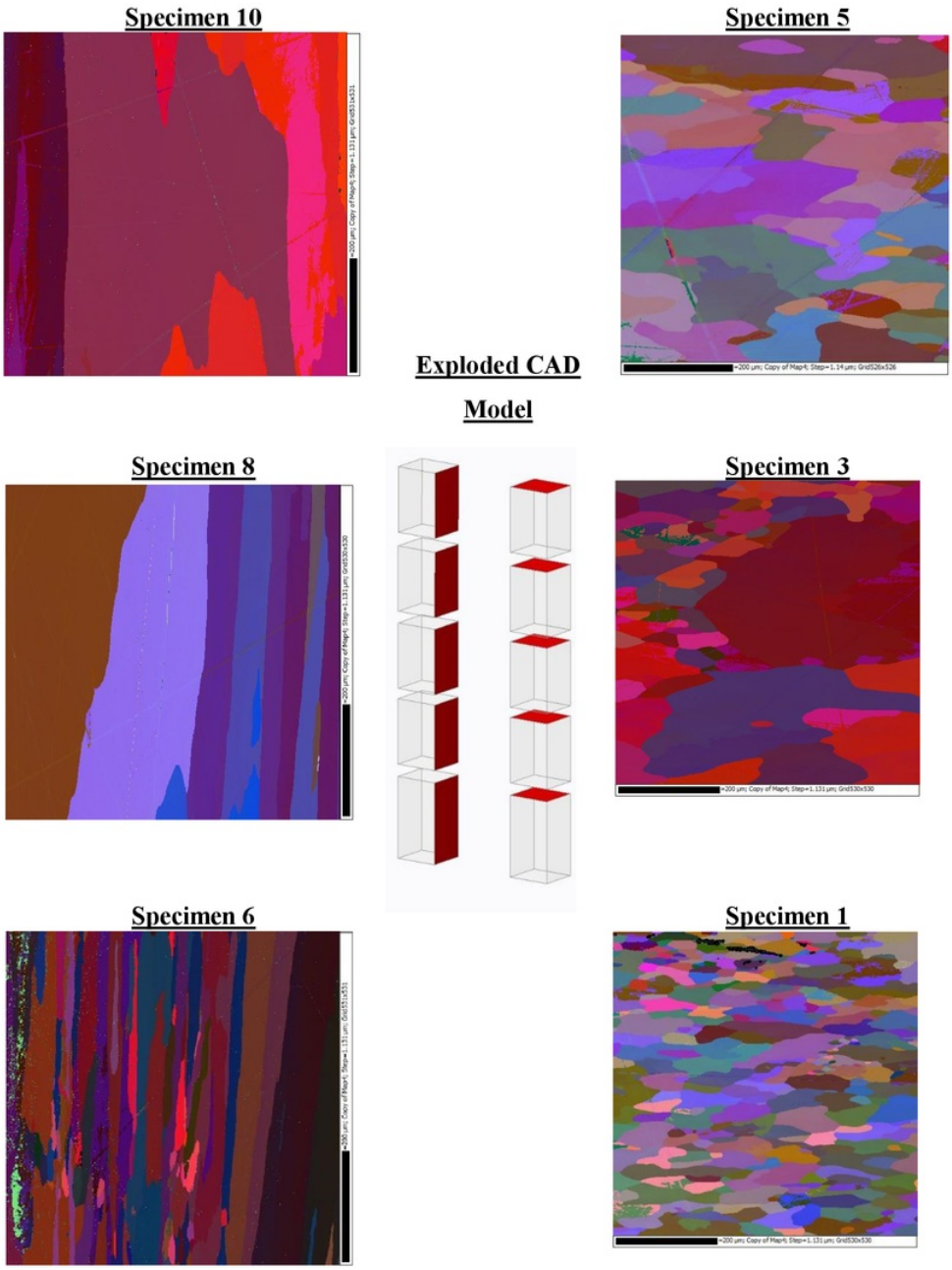

Figure 23: Schematic of the microstructure obtained from the investigation for the various specimens

Table 3: Grain Area Averages and Standard Deviations for each part along the various

	Part 1	Part 3	Part 5	Part 6	Part 8	Part 10
Average Area (µm²)	1010.142	3185.912	5401.43	2611.193	19397.91	21675.39
StDev Area (µm²)	1190.66	7535.121	8570.434	5880.984	25573.61	17549.75

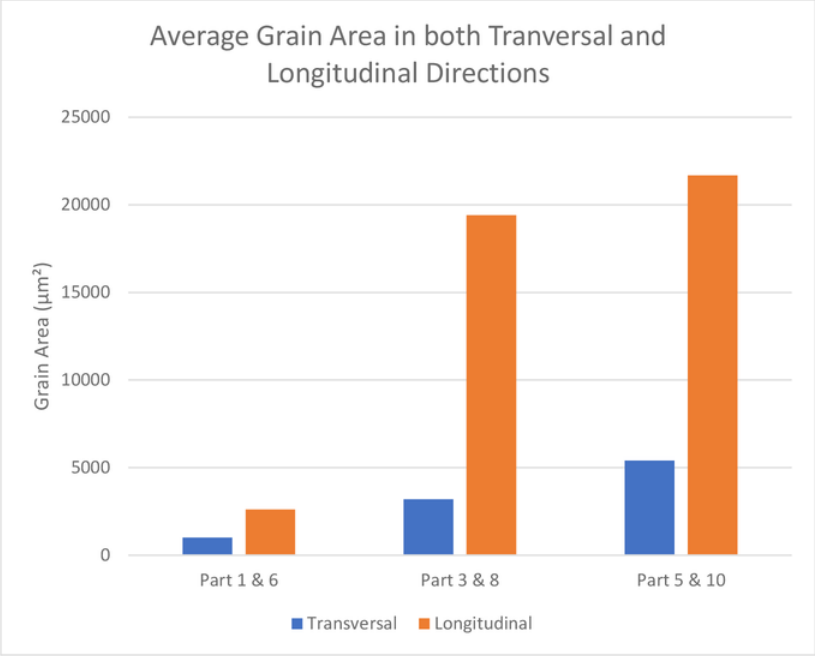

Figure 24: Average Grain Area in both Transversal and Longitudinal Directions

Figure 23 clearly shows the essential comparisons between both the latitudinal/transversal and longitudinal cross-sections as well as along the varying heights.

It is observed from the figure that specimens 6-10 which have been prepared respective to the longitudinal cross-section flaunt a columnar crystal grain structure, which contrasts with the specimens 1-5, whom possess a much more equiaxed morphology in comparison. Table 3 validates a quantified difference between the transversal and longitudinal sections. Around the same height variation, the data obtained suggests that there is indeed an average of smaller sized crystal grains within the transversal direction of cut to that of the longitudinal cut. The

data indicates that for the transversal cut in specimen 1, there is an average crystal grain size of 1010.142μm². Comparing this to the longitudinal cut in specimen 6 for the similar height, indicates an average crystal grain size of 2611.193μm². Likewise, if all the other specimens were compared together as well, the evaluation leads to deducing that there is indeed an average of smaller sized crystal grains within the latitudinal cross-sectional cut than those crystal grains of a longitudinal cross-sectional cut. This trend is presented in the graph in figure 24, where the various similar heights are grouped together and compared against their average grain size. For example, specimen 3 in comparison to specimen 8 has an average crystal grain size of 3185.91 μm² and 19397.91μm² respectively, along with specimen 5 and 10 which have an average crystal grain size of 5401.43μm² and 21675.39μm² respectively.

The crystal grains are much larger in the vertical than in the horizontal cross-section due to many reasons. The literature suggests that the deposited material will follow columnar growth near the center of the melt pools, the melt pool keeps increasing as the more material is deposited layer by layer in increase of the height. Hence this is the case for our longitudinal sectioned cuts, they are observed to have a columnar crystal grain structure corresponding to the melt pools formed during deposition. The latitudinal sectioned cuts are observed to have a more textured crystal grain orientation due to the deposited droplets solidifying within the direction of print, this solid to liquid transition produces an array of distinct thermal gradients which generates directional textured microstructures. Specimens 6-10 are perceived to follow a columnar crystal grain flow, following the direction of elongation in the z direction.

Furthermore, with a difference observed in both horizontal and vertical cross-sections, there is another notable change in the microstructure with the varying heights of the 3D printed part. It is comprehended from the EBSD patterns attained from the SEM for each specimen that as the height increases for the printed part, the number of crystal grains of each decreased and hence accordingly the grain size increased as a result. The increase in grain size is shown in the crystal grain analysis table (Table 3), where in the longitudinal cross-section from part 6 to part 8 then part 10 there was an increase from an average grain size of 2611.19μm² to 19397.91μm² then 21675.39μm² respectively. There was also an observed increase in the transversal cross-section crystal grain size depicted by the data obtained in Table 3, where from part 1 to part 3 to part 5 the crystal grain size increased from 1010.14μm² to 3185.91μm² to 5401.43μm².

This increase in crystal grain size is expected and follows the literature, this is due to the fact that during when the part is being manufactured, each deposited particle first is solidified when

it gets in contact with the previously solidified material or the substrate after creating a melt pool with a heat affected zone. Since this is a layer by layer addition process, the heat affected zone created by the melt pool for the newly deposited section interacts with the previous layer at the same point and the layer before that perhaps, and this constant heat addition process to the previously deposited layer which is being slowly cooled by the air surrounding the material allows for the heat treatment of the part around that section, which carries on moving to the next section in the direction of travel. This heat treatment of the part can be deduced to be of the annealing phenomenon, which is the heat addition process to a previously manufactured component, then slowly cooled to change the property of that part by changing the internal microstructure of the part.

The annealing heat treatment process allows for the internal structural grains to be recrystallised due to the slow cooling rate after the heat addition printing process. The cooling rate at the interface is much quicker than the cooling rate at the highest layer which was printed. This is the case since the part is 3D printed onto the substrate, the substrate already is fully cooled down and at the same temperature as the surrounding environment, therefore the interaction of the melted 316L stainless steel which is being printed with the substrate will allow for a more rapid cooling of the deposited material. The heat affected zone close to the interface of the substrate and deposited metal is considerably small due to the surface tension and residual stress and instead the thermal effect of the melt pool will spread around the beam path. As more layers of the part is printed layer by layer the cooling rate slowly decreases as well, this is for the reason that as you print layer by layer the heat affected zone which will be produced from the melt pool will increase in size as the layer beneath the one you are printing on is not fully cooled yet. The higher you go from the interface the higher the heat affected zone is. Near the interface the cooling was rapid due to the temperature difference between both the melted metal and the substrate being much higher than that as you go higher due to the constant heating of the layer by layer addition process. As stated in the literature, the higher cooling rates lead to a decrease of ferrite grain size and formation of high strength, hardness, dislocation density, and fine phases because it suppresses the atomic diffusion. Whereas slow cooling rates lead to transformation into soft, coarse and less dislocated phases like polygonal ferrite.

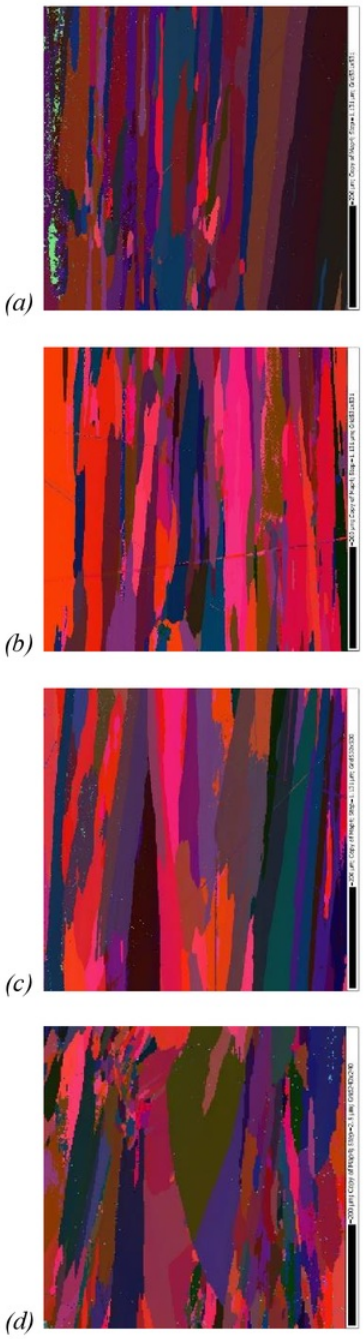
(a)
(b)
(c)
(d)
б
(a)
(b)
(c)
(d)

Figure 25: Part 6 different sections with a schematic (a) Top -2mm (b) About halfway (c) Interface +2mm (d) Close to Interface

Table 4: Crystal grain data obtained for various sections of Part 6

	(a)	(b)	(c)	(d)
Average Area (µm²)	1010.142	1577.181	4887.948	1451.254
StDev Area (µm²)	1190.66	3625.291	6382.328	3603.799

Figure 25 above shows the results obtained from various sections of part 6 and how each depict the phenomenon discussed before in a smaller setting. Part 6 was loaded into the SEM and various sections of the part were examined using their corresponding EBSD patterns. Section (a) of part 6 portrays the crystal orientation of the grains at approximately 2mm below the top of the part. Section (b) reveals the grain structure of part 6, approximately half way through the part. Section (c) interprets the crystal grain orientations for approximately 2mm above the interface of part 6. Lastly section (d) depicts the crystal structure observed close to the interface.

These sections presented together in figure 25 allows us to visualise that closer to the interface, the crystallography is observed to be very random with smaller grains closer to the interface, increasing in size as the height increases. Going towards heighest section, section (a), it is also observed that the grain structure of the part is leading towards a more columnar structure with slight variations in the structure between sections (b) & (c).

Table 4 does not technically show a relationship in varying height means a varying average size of grain, but it does show the random structure of the grains closer to the surface due to the higher cooling rate.

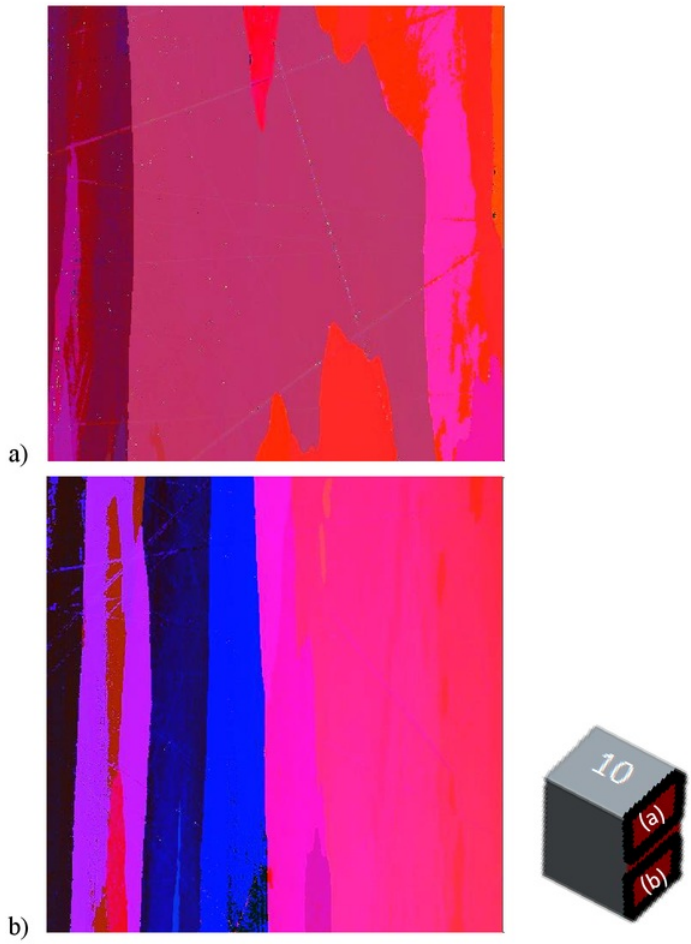

Figure 26: Part 10 (a)Top -2mm (b)Bottom +2mm

Table 5: Grain analysis data obtained from different sections of part 10

	(a)	**(b)**
Average Area (µm²)	21675.39	21660.71
StDev Area (µm²)	17549.75	17567.82

Figure 26 above focuses on the results obtained regarding part 10 of the manufactured sample. Part 10 is the highest part in the longitudinal cross-sectional cut, hence this is the highest section which can be examined regarding the cooling rate affecting the microstructural grain structure. Part 10 is divided up into 2 sections, section (a) portrays the crystal grain structure 2mm from the top and section (b) interprets the internal crystal structure 2mm from the bottom.

Section (b) in figure 26 emphasises large elongated longitudinal grains in the direction of the heat treatment process parellel to the build direction going up. In comparsion to the heighest section, section (a), the crystal grains appear to be slightly smaller, but still follows a columnar grain structure. Section (a) contains crystal grains within it, that are much larger than the frame hence accurate values for the grain sizes are not found, yet still it is deduced that this section of the part also follows a columnar grain structure with grains larger than that from the bottom section of part 10, section (b). This can be verfied using Table 5 above, comparing the average grain sizes of each section in the part.

In the figure above it is evidently observed that as the height of the sample increases, the crystal grains also increase in size. The grains are seen to be of more equiaxed morphology as the specimens go higher. The results obtained demonstrated that between the longitudunal and horizontal cross-sectional, there was indeed a clear difference in terms of grain structure. Section (a) was observed to have an average grain size of 21675.39μm^2 while section (b) demonstrated having an average crystal grain size of 21660.71μm^2, hence suggesting that the higher section comprised of larger sized grains.

All the various parts of the sample obtained data from the SEM and the additional attachement to reveal each section's crystal grain structure which was presented in figures 23-26 highlighted some discrepancies. Each of the patterns presented above, showcased each corresponding sections internal orientations, but mostly all of them possessed some surface defects. These defects can include scratches, pores and other abnormalities which cause for missing information when carrying out the EBSD analysis.

To overcome this problem, a software program was used to assign these missing points of information to a value which was extrapolated from the neighbouring points. These allocation of values and extrapolation, might affect the overall final result which is obtained, as these imperfections on the surface can change the crystal grains which were counted by the system and hence their total grain areas will be affected as well correspondingly.

As stated before as well, some of the patterns obtained from each of the parts exposed grains which were not completely within the frame which was scanned. The higher dimensioned frames were not practical to use for electron back scatter scanning due to time constraints as well as feasibility issues. This suggests that within the frame the total size of the whole grain was not calculated within the results as it lies outside the frame of scan, hence the results will possess some discrepancy and a definite deduction can not be made quantificationally.

In terms of comparing both the reference 316l stainless steel rod and the 3D printed 316L stainless steel part, it is clearly evident that there is indeed a difference between both the manufacturing methods. The reference rod observed no considerable differences in both the latitudinal and longitudinal cross-sections in terms of the internal crystal grain structure, in contrast the 3D printed part was observed to contain an evident difference between both cross-sections. Along with that the microstructural analysis between the 2 manufacturing methods indicate that the conventional methods boast an equiaxed and angular crystal orientation, where else the printed part was shown to have a columnar structure which elongated and increased each grain in the longitudinal cross section while in the lattitudinal cross-section it was observed to be a more textured crystal grain orientation which also increase in size with increasing height due to the varying cooling rates of the part. The various cooling rates drove grain growth, this developed ferritic and pearlitic microstructures depending on the cooling rate which allows for the material to possess various mechanical properties with varying heights.

5. Conclusion

This study was successful in satisfying the aim to investigate the microstructures of the final 3D printed 316L stainless steel and compare it to the traditional/conventional method of manufacturing being carried out currently.

Microstructural analysis was undertaken for both the reference sample as well the 3D printed sample. The results obtained highlight that there is an overall difference when comparing both the methods of manufacturing. The reference 316L stainless steel rolled rod was compared to a 3D printed 316L stainless steel manufactured part in terms of their internal crystal orientations. The reference rod was observed to have negligible variations in the latitudinal and longitudinal cross-sections, as both illustrated an equiaxed morphology which was quite angular in grain structure. This was in contrary to the manufactured 3D printed 316L stainless steel part, which demonstrated that there were indeed variations in both the latitudinal and longitudinal cross-sections along with a change in the internal crystal grain structure with the change in height, due to the fluctuations in cooling rates as you go higher in the build direction. Hence it is deduced that cooling rate does indeed drive the grain size.

The information described in this study should be taken into account for when designing components, parts or assemblies. The design of each can be implemented by the various conventional methods of production or the emerging additive manufacturing option, they both have their various advantages and disadvantages, but corresponding to the application of the product the suitable manufacturing method should be incorporated according to the material presented within this study.

6. Future Work

In the research which has been conducted up till date, the results obtained did indeed fulfil the qualification purpose of highlighting the various differences between various manufacturing methods, showcasing the dynamics of the different mechanisms for each crystal grain orientation.

Further Research into the quantification and further qualification into explaining why the results which are obtained are the outcomes of this process. A more in-depth research into this varying phenomenon will achieve this.

This work has summarised the potential of 3D printing of metals and their alloys for various geometries according to the unique properties they possess, corresponding to the microstructures and structural features. Due to the asymmetric temperature gradients at the various heights of the sample which has been 3D printed, as hypothesised the material will be developed differently with varying properties due to the faster cooling rates. Future work in preventing this variation will be beneficial for the overall structural homogeneity, stability and reliability throughout the structure being constructed.

7. Nomenclature

AM	Additive Manufacturing
CAD	Computer Aided Diagram
CSIRO	Commonwealth Scientific and Industrial Research Organisation
DLD	Direct Laser Deposition
EBSD	Electron Back Scattering Diffraction
HAZ	Heat Affected Zone
LBAM	Laser Based Additive Manufacturing
SEM	Scanning Electron Microscope
SLM	Selected Laser Melting
SLS	Selected Laser Sintering
UTS	Ultimate Tensile Strength

8. References

[1] B. Conner, G. Manogharan, A. Martof, L. Rodomsky, C. Rodomsky, D. Jordan and J. Limperos, "Making sense of 3-D printing: Creating a map of additive manufacturing products and services", *Additive Manufacturing*, vol. 1-4, pp. 64-76, 2014.

[2] D. Wang, S. Wu, Y. Bai, H. Lin, Y. Yang and C. Song, "Characteristics of typical geometrical features shaped by selective laser melting", *Journal of Laser Applications*, vol. 29, no. 2, p. 022007, 2017.

[3] S. M. MUKHOPADHYAY, "Sample Preperation for Microscopic Evaluation," 2003

[4] K. J. Christiyan, "A study on the influence of process parameters on the Mechanical Properties of 3D printed ABS composite," IOP Conference Series: Materials Science and Engineering, vol. 114, p. 012109, 2016.

[5] N. A. A. Osman, "Effect of Layer Thickness and Printing Orientation on Mechanical Properties and Dimensional Accuracy of 3D Printed Porous Samples for Bone Tissue Engineering," PLoS ONE, vol. 9, no. 9, p. e108252, 2014.

[6] D. Wang, S. Wu, Y. Bai, H. Lin, Y. Yang and C. Song, "Characteristics of typical geometrical features shaped by selective laser melting", *Journal of Laser Applications*, vol. 29, no. 2, p. 022007, 2017.

[7] S. M. Thompson, "An Overview of DLD for addiditive manufacturing;," Part I: Transport Phenomena, Modeling and Diagnostics, pp. 36-62, 2014.

[8] "EBSD Oxford Instruments - Introduction", *Ebsd.com*, 2017. [Online]. Available: http://www.ebsd.com/introduction.

[9] "EBSD Oxford Instruments - The Diffraction Pattern", *Ebsd.com*, 2017. [Online]. Available: http://www.ebsd.com/ebsd-for-beginners/12-ebsd-for-beginners/51-the-diffraction-pattern.

[10] Kumar, S. and Pityana, S. (2011). Laser-Based Additive Manufacturing of Metals. *Advanced Materials Research*, 227, pp.92-95.

[11] W. Zhou, *Advanced scanning microscopy for nanotechnology*. New York, NY: Springer, 2007.

[12] S. Swapp, "Electron Backscatter Diffraction (EBSD)", *Geochemical Instrumentation and Analysis*, 2017. Available: https://serc.carleton.edu/research_education/geochemsheets/ebsd.html

[13] H. Li, Z. Qu, Q. Zhao, F. Tian, D. Zhao, Y. Meng and X. Lu, "A reliable control system for measurement on film thickness in copper chemical mechanical planarization system", *Review of Scientific Instruments*, vol. 84, no. 12, p. 125101, 2013.

[14] M. Matthews, G. Guss, S. Khairallah, A. Rubenchik, P. Depond and W. King, "Denudation of metal powder layers in laser powder bed fusion processes", *Acta Materialia*, vol. 114, pp. 33-42, 2016.

[15] L. Murr, E. Martinez, K. Amato, S. Gaytan, J. Hernandez, D. Ramirez, P. Shindo, F. Medina and R. Wicker, "Fabrication of Metal and Alloy Components by Additive Manufacturing: Examples of 3D Materials Science", *Journal of Materials Research and Technology*, vol. 1, no. 1, pp. 42-54, 2012.

[16] R. Manna, "Time Temperature Transformation (TTT) Diagrams", *Phase trans.msm.cam.ac.uk*, 2017. [Online]. Available: https://www.phase-trans.msm.cam.ac.uk/2012/Manna/Part2.pdf.

[17] M. Equbal, P. Alam, R. Ohdar, K. Anand and M. Alam, "Effect of Cooling Rate on the Microstructure and Mechanical Properties of Medium Carbon Steel", *International Journal of Metallurgical Engineering*, pp. 21-24, 2017.

[18] "Metastable Iron-Carbon (Fe-C) Phase Diagram", *Calphad.com*, 2017. [Online]. Available: http://www.calphad.com/iron-carbon.html.

[19] C. Kwan and Z. Wang, "Microstructure evolution upon annealing of accumulative roll bonding (ARB) 1100 Al sheet materials: evolution of interface microstructures", *Journal of Materials Science*, vol. 43, no. 15, pp. 5045-5051, 2008.